Density functional calculations for Zintl systems: structure, electronic structure and electrical conductivity of liquid NaSn alloys

1998 J. Phys.: Condens. Matter 10 1175

(http://iopscience.iop.org/0953-8984/10/6/002)

J. Phys.: Condens. Matter **10** (1998) 1175–1198. Printed in the UK PII: S0953-8984(98)86986-5

Density functional calculations for Zintl systems: structure, electronic structure and electrical conductivity of liquid NaSn alloys*

G Seifert†, R Kaschner†, M Schöne† and G Pastore‡

† Technische Universität Dresden, Institut für Theoretische Physik, D-01062 Dresden, Germany
‡ Istituto Nazionale di Fisica della Materia and Dipartimento di Fisica Teorica dell' Università, Strada Costiera 11, I-34014 Trieste, Italy

Received 20 August 1997, in final form 5 December 1997

Abstract. Molecular dynamics (MD) simulations are presented for five different compositions of liquid NaSn alloys, covering the range from 20 to 80% sodium. We apply an *ab initio* (Car–Parrinello) method as well as an approximate LCAO-DFT scheme. The two methods yield similar results: the tin atoms form large dynamic networks. Only for the sodium-rich composition are isolated tin atoms and dimers observed.

From the *ab initio* MD trajectories the structure factors, the total and partial densities of states, the charge distributions and, by means of the Kubo–Greenwood formula, the electrical conductivities are calculated. The structure factors and the conductivities are obtained as functions of the composition and show good agreement with experimental data.

We give a detailed discussion of the concentration dependence of the structure factors, the total and partial densities of states, the charge distributions and the electrical conductivities. The behaviour and the origin of the prepeak is discussed. For the equimolar composition the dependence of the conductivity on temperature is obtained and is in qualitative accord with experimental data.

1. Introduction

Zintl compounds are a very interesting class of systems which have been under investigation, experimentally as well as theoretically, for a long time, with increasing activity in recent years. In general, they are binary systems which contain the so-called 'Zintl ions'. These (an)ions are isovalent to typical neutral molecules or clusters and exhibit some of their properties—according to the Zintl (or Zintl–Klemm) concept [1]. In particular, these ions have the same geometries as their isovalent counterparts. A comprehensive overview of Zintl-type systems was published very recently [2].

One typical example of Zintl systems is constituted by alloys of alkaline metals and group-IV elements. In the equimolar case, the group-IV atoms (B) form tetrahedral anions B_4^{4-}. These Zintl anions get their fourfold negative charge from the four surrounding alkaline atoms and are isovalent to the neutral P_4 molecule, which is a tetrahedron, too.

Liquid Zintl alloys played a central role in the development of models for compound formation (anion clustering) in liquid anionic alloys [3–5]. Interesting questions and quantities relevant to such liquid alloys are: the structure (behaviour of the Zintl ions in

* Dedicated to Professor H O Lutz on the occasion of his 60th birthday.

0953-8984/98/061175+24$19.50

the melt), the structure factors and the electrical conductivity as a function of composition and temperature. In the last few decades such alloys have been investigated experimentally as well as theoretically; a review of Zintl ions in many different liquid alloys was given recently [6]. Older work concerning liquid alkali–lead alloys dealt (for example) with neutron diffraction measurements [7] and model calculations [8]; but there have also been recent model studies [9].

A very successful tool for describing condensed matter properties is *ab initio* molecular dynamics simulation. From the calculated trajectories one can extract structural properties as well as data concerning the electronic structure, including, for example, conductivities.

In the last few years, theoretical investigations using *ab initio* molecular dynamics methods have been performed for several liquid alloys, such as K–Si [10], Li–Si [11], Cs–Pb [12], Mg–Bi [13], Ga–Se [14] and Ag–Se [15].

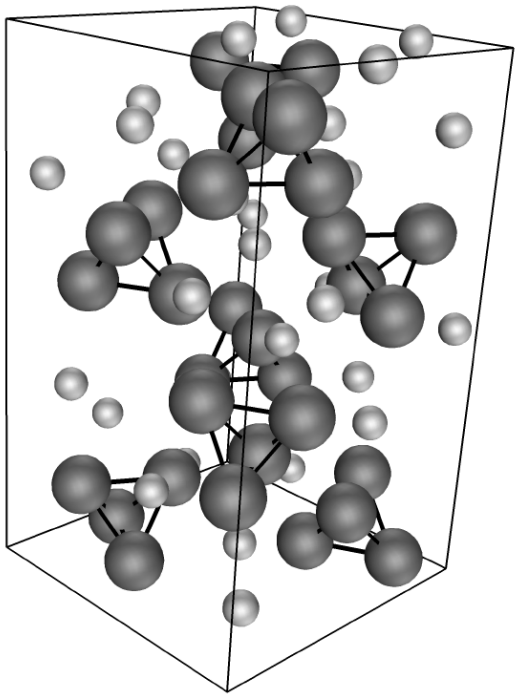

Figure 1. The structure of solid β-NaSn, after Müller and Volk [17].

In this paper we consider the liquid alloys of sodium and tin, which show the anion clustering mentioned above; for a review see [16]. The Zintl ions in the equimolar solid β-NaSn are Sn_4^{4-} tetrahedra; see reference [17] and figure 1. The electronic structure of the solid (equiatomic) NaSn alloy was discussed theoretically using the ASW method [18]. Theoretical work on liquid NaSn alloys in the last decade was confined to simple models only [5, 16, 19]. On the other hand, much experimental work on these alloys has been done even in the last few years [20, 21].

We were the first to apply an *ab initio* method to such a liquid Zintl alloy. In a first letter [22] the structural properties of the equimolar composition were investigated: the static structure factors and the stability (network formation) of Zintl ions for liquid equimolar NaSn were discussed. In a second letter [23] these investigations were extended to a set of five

compositions ranging from 20 to 80% sodium. In a recent publication [24] we presented the electrical conductivity for these systems, calculated using the Kubo–Greenwood scheme [25], and discussed the electronic densities of states. Reference [24] was the first work to present the *concentration dependence* of the conductivity of Zintl alloys from first-principles calculations.

The purpose of the present publication is to complete the discussion of the conductivities with their temperature dependence, to summarize the previous results and to discuss them more extensively in combination with the charge distributions. Furthermore, we give a more detailed discussion of the structures and the prepeak of the structure factor.

For the MD we apply two methods: (i) the Car–Parrinello method [26], which is a scheme for fast *ab initio* molecular dynamics simulations; and (ii) a simplified LCAO method [27], which allows one to treat larger systems, to realize longer simulation times and to calculate atomic charge densities and partial densities of states in a simple way.

This paper is organized as follows. In section 2 we describe both methods. Afterwards, the details of the calculations are presented. Section 4 gives a discussion of the results obtained, such as structures, static structure factors, densities of states, charge distributions and electrical conductivities. Our discussion will mainly focus on results from the *ab initio* (CP) calculations. Finally, a summary and an outlook are given.

2. Methods

2.1. The Car–Parrinello method

The Car–Parrinello (CP) method [26] is an *ab initio* scheme for molecular dynamics simulations in which the electronic contribution to the interatomic forces is evaluated within density functional theory. This method allows efficient molecular dynamics (MD) calculations due to the introduction of a fictitious dynamics for the electronic wavefunctions (Ψ_i) which is performed simultaneously with the dynamics of the nuclei. Thus the system is kept close to the Born–Oppenheimer surface without there being any need to perform time-consuming SCF loops after each MD step to keep the system in its electronic ground state.

Minimizing the Kohn–Sham energy functional (E) within the framework of the classical Lagrange formalism generates equations of motion for the fictitious electron dynamics:

$$\mu\ddot{\Psi}_i(\boldsymbol{r}) = -\frac{\delta E}{\delta \Psi_i^*(\boldsymbol{r})} + \sum_j \Lambda_{ij}\Psi_j(\boldsymbol{r}) \tag{1}$$

where the Λ_{ij} are Lagrange multipliers ensuring the orthonormality of the electronic wavefunctions Ψ_i.

The nuclei are moved applying the usual Newton dynamics:

$$M_i\ddot{\boldsymbol{R}}_i = -\frac{\partial E}{\partial \boldsymbol{R}_i}. \tag{2}$$

The charge density is obtained from the wavefunctions by using the well-known expression from Kohn–Sham theory

$$\rho(\boldsymbol{r}) = \sum_i n_i|\Psi_i(\boldsymbol{r})|^2 \tag{3}$$

where the n_i are the occupation numbers.

The forces are calculated using the Hellmann–Feynman theorem. This can be done without additional (Pulay) terms, as the wavefunctions are expanded in plane waves:

$$\Psi_i(\boldsymbol{r}) = \sum_k c_k^i \mathrm{e}^{-\mathrm{i}\boldsymbol{K}\cdot\boldsymbol{r}}. \tag{4}$$

The CP simulations were performed using the MOTECC-90 computer code [28].

The exchange–correlation potential was used in the local density approximation (LDA) on the basis of the expression of Perdew and Zunger [29] which fits the quantum Monte Carlo results. We applied the pseudopotentials of Bachelet *et al* [30]. For the Brillouin zone sampling in the calculation of the charge density we used the Γ-point approximation; due to the large supercell and the number of atoms in it, the phase-space volume per state is such that the k-sampling using the Γ point only gives most of the relevant system information. For simple metals, for example pure sodium, such an approximation may lead to significant errors—see e.g. [31], but for the systems considered here only small deviations are to be expected.

To determine the cut-off energy for the plane-wave basis set in equation (4), we performed several tests.

(i) We calculated the equilibrium bond lengths of Na_2, Sn_2 and NaSn dimers with different cut-off energies and large supercells. These data were compared with experimental data [32] and with results obtained by means of an *ab initio* all-electron SCF (self-consistent-field) LCAO-DFT code [33]—within the LDA and also including gradient corrections (GC); see also [23]. Generally, using a nearly converged plane-wave basis, the interatomic distances that are obtained are about 5–7% smaller than those from all-electron DFT-LDA calculations and the experimental values. Hence, that deviation must be attributed to the pseudopotentials—especially the frozen-core approximation and the neglect of the so-called non-linear core corrections [34]. The effect of the gradient corrections is small compared to this deviation.

(ii) Similar tests were performed for the bulk cells of crystalline sodium and tin, respectively. The lattice constants for the equilibrium geometries obtained converge in a similar manner to the cut-off energy and show the same trend (about 5–10% smaller than the experimental values) as the dimer bond lengths.

Consequently, the plane-wave cut-off was chosen to be 6 Ryd.

2.2. The LCAO method

In addition to the CP method we applied a simplified LCAO method [27] for our MD simulations which is based on density functional theory and the LDA, too. (Note that this scheme is different from the SCF-LCAO method [33] mentioned above!) It provides a very fast and reliable alternative to SCF methods and allows the use of larger supercells with more atoms. Among its advantages is the ease with which atomic charges (via a Mulliken population analysis [35]) and partial densities of states can be obtained.

The method is described in detail in reference [27]. It is a 'hybrid' between *ab initio* and empirical methods and can also be viewed as a *density-functional-based tight-binding (TB) scheme*: the Hamiltonian has the same form as in non-orthogonal TB theory. Corresponding to the usual TB energy expression, the total energy within our LCAO method is written as

$$E_{tot} = \sum_i^{occ} \varepsilon_i + \frac{1}{2}\sum_j \sum_{\substack{j' \\ j\neq j'}} U(R_{jj'}) \tag{5}$$

where the ε_i are the solutions of the secular equation

$$\sum_{\mu} c_{\mu}^{i}\{H_{\mu\nu} - \varepsilon_i S_{\mu\nu}\} = 0 \tag{6}$$

with c_{μ}^{i} being the wavefunction expansion coefficients.

However, unlike in traditional parametrized TB schemes, here the Hamiltonian ($H_{\mu\nu}$) and overlap ($S_{\mu\nu}$) matrix elements are calculated *from first principles*.

This is done using a set of atomic basis functions, which are obtained from self-consistent atomic LDA calculations.

The effective Kohn–Sham potential within the Hamiltonian is approximated by a superposition of the potentials of neutral atoms. Here only one- and two-centre integrals are taken into account.

For each atomic configuration one has to solve the secular equation (6) (which is in fact a set of algebraic equations) once. Hence this method is very fast, allowing, in particular, efficient MD simulations with long simulation times.

For each atomic combination (in our case: Na–Na, Na–Sn, Sn–Sn [36]), the repulsive pair potential $U(R_{jj'})$ in the energy expression (5) is determined as a universal short-ranged potential $U_{AB}(R)$ from fits to SCF data (from the SCF-LCAO code [33]) for the corresponding dimers.

3. Calculations

3.1. Systems and temperatures

The MD simulations discussed in this paper were performed with supercells containing 64 atoms for the CP-MD and 64 as well as 216 atoms for the LCAO-MD.

The starting point for each simulation was the geometry of solid β-NaSn as described in [17] (cf. figure 1). First we rescaled this orthorhombic supercell (with 64 atoms) to a cubic cell, keeping the volume (and density) the same, i.e. with the cell length of 23.4 au, and leaving the Sn_4^{4-} tetrahedra intact. So, we used a cell with the experimentally known density of the solid containing the Zintl tetramer anions Sn_4^{4-} as described in the introduction.

Starting with this equimolar system, we generated different compositions by replacing Na by Sn atoms or vice versa at the same atomic positions. The volume contraction connected with this change of composition can be calculated by means of simple semi-empirical rules [37, 38]. As they predict little change in volume, we took the same cell volume for all cases.

For our investigations we selected compositions for which experimental structure factor data were given in [16]: 20, 40, 50, 57 and 80% sodium—corresponding to the following 64-atom supercells: $Na_{13}Sn_{51}$, $Na_{26}Sn_{38}$, $Na_{32}Sn_{32}$, $Na_{36}Sn_{28}$, $Na_{52}Sn_{12}$. We performed *Car–Parrinello* and LCAO-MD simulations with these systems as described below.

For the three tin-rich compositions we constructed equivalent supercells with 216 atoms each and performed LCAO-MD simulations. To keep the density constant the cell size was selected to be 35.1 au. The enlarged supercells were obtained by applying a periodic continuation of the original ones in each direction and cutting out the desired cubic cell. Furthermore, we have chosen the larger cell such that all Zintl tetrahedra were left intact. That is, we started both CP and LCAO simulations with equivalent supercells of different sizes, so that the two simulations can be compared directly.

Additionally, we performed for the equimolar case an LCAO-MD simulation with the 'original' orthorhombic supercell containing 64 atoms as taken from [17].

The temperatures of the MD simulations represent averages of the kinetic energies of the ionic systems over the whole trajectories. Their fluctuations are about ± 100 K. They were chosen to be approximately the same as the ones for which the structure factors were measured. In general these neutron scattering experiments were performed at about 25 K above the liquidus point of the corresponding composition. Only for the 20% Na case was the temperature for the experiment considerably larger. The temperatures of the simulations (T_{MD}) and the experiments (T_{exp}) [16] are given together with the corresponding liquidus points [39] in table 1.

Table 1. Systems and temperatures for the CP simulations. For each system the averaged temperature $\bar{T}_{MD}$ of the simulation is compared to the temperature T_{exp} for which the neutron scattering experiments in [16] were performed. In addition the liquidus temperature T_{liq} is given [39].

Supercell	Atomic % Na	$\bar{T}_{MD}$ (K)	T_{exp} (K)	T_{liq} (K)
$Na_{13}Sn_{51}$	20.3	726	723	580
$Na_{26}Sn_{38}$	40.6	818	813	783
$Na_{32}Sn_{32}$	50.0	921	873	851
$Na_{36}Sn_{28}$	56.3	796	778	752
$Na_{52}Sn_{12}$	81.3	748	713	681

3.2. The simulation procedure

At the beginning of the simulation the nuclei were shifted slightly by a random displacement. After this, the nuclei were relaxed by means of a steepest-descent technique for the electronic and ionic systems.

Afterwards, the system was equilibrated in order to obtain the desired average temperature. The system was heated to a finite temperature by rescaling the velocities of the nuclei. Then the MD was performed for about 1000 steps. After that the velocities were rescaled again to the desired temperature, and this 'heating-equilibration' process was repeated until the averaged temperature over an MD run of about 5000 steps reached the desired value within ± 50 K.

That is, the MD simulations were performed for a microcanonical ensemble: constant energy and volume, without a heat bath.

For the CP dynamics, the parameters μ—the fictitious mass of the electronic states (orbitals); see equation (1)—and δt—the time step of the MD—were optimized during this 'heating-equilibration' process: the kinetic energy of the electronic states had to be monitored to check that it remained small and constant. A too large μ would invoke oscillations in the electronic subsystem with frequencies comparable to those of the ionic motion and thus open up an efficient channel for an energy transfer into the electronic subsystem. As a consequence the system would depart from the Born–Oppenheimer (BO) surface, producing unphysical dynamics of the nuclei.

To provide a numerically stable integration of the electronic equations of motion, $\delta t^2/\mu$ had to be chosen not too large. Thus, δt had to decrease with μ.

On the other hand the time step δt had to be large enough for us to obtain a total MD simulation time which allows the extraction of the desired physical quantities of the liquid.

For the LCAO dynamics, the optimization of δt was easier. Here the only condition that had to be obeyed was that δt was not too large—to allow a numerically stable finite-step simulation of the nuclear motion.

In particular, we obtained the following optimized ranges for these parameters: for the CP method: $\delta t = 5$–10 atu (1 atu $= 2.4 \times 10^{-17}$ s), $\mu = 300$–500 electronic masses; and for the LCAO method: $\delta t = 50$ atu.

Finally, for the collection of the data, 'production runs' were performed with at least 10 000 steps of CP-MD or at least 2000 steps of LCAO-MD, respectively—corresponding to a total simulation time of about 2 ps. This time is long enough to obtain a description for the fluctuations of the interatomic distances. However, this time is too short for simulating a real melting process. Instead, we checked the 'liquidity' of the system during all MD runs by monitoring the time dependence of the mean square displacement of the atoms from their starting positions: for a bulk liquid, after an initial transient, this quantity has to increase linearly with the simulation time.

Each 'production run' yields a phase-space trajectory of the system considered. An average over this trajectory corresponds to a thermal average of a microcanonical ensemble. From this trajectory all quantities of interest can be extracted—as described in the following subsections.

In section 4 we will focus on the results from the Car–Parrinello (*ab initio*) MD simulations. The final averaged temperatures of the CP 'production runs' are given above in table 1.

3.3. Structure factors

The static structure factors can be calculated from the atomic positions of the MD trajectory as described e.g. in [16, 40]. Here we summarize only the essential ideas.

The total structure factor $S(q)$ (which is proportional to the measured intensity $I(q)$ from neutron scattering experiments, where $\boldsymbol{q}$ denotes the scattering vector) has—according to Ashcroft and Langreth [40]—for a two-component system the following form:

$$S(q) = \sum_{\alpha} \sum_{\beta} c_\alpha c_\beta \frac{b_\alpha b_\beta}{\langle b^2 \rangle} S_{\alpha\beta}(q) \tag{7}$$

with α and β each standing for the two species (Na and Sn), where c_α is the concentration and b_α the neutron scattering constant of species α. $\langle b^2 \rangle$ is the average of b_α^2 over all of the atoms of the supercell.

$S_{\alpha\beta}(q)$ is the partial structure factor of species α and β, which is related to the corresponding pair correlation function $g_{\alpha\beta}(r)$ via Fourier transformation. The partial structure factors are obtained directly from the nuclear positions via (for $q \neq 0$)

$$S_{\alpha\beta}(q) = \frac{1}{N_\alpha N_\beta} \left\langle \sum_{\alpha}^{N_\alpha} \sum_{\beta}^{N_\beta} \mathrm{e}^{-\mathrm{i}\boldsymbol{q}\cdot(\boldsymbol{R}_\alpha - \boldsymbol{R}_\beta)} \right\rangle. \tag{8}$$

N_α is the number of atoms of species α per unit cell and the $\boldsymbol{R}_\alpha$ are the positions of these atoms; the brackets indicate an average over the whole MD trajectory.

An alternative way to split up the total structure factor was proposed by Bhatia and Thornton [41]. Their structure factors are related to the Ashcroft–Langreth structure factors $S_{\alpha\beta}(q)$ as follows:

$$S_{NN}(q) = c_1 S_{11}(q) + c_2 S_{22}(q) + 2c_1^{1/2} c_2^{1/2} S_{12}(q) \tag{9}$$

$$S_{NC}(q) = c_1 c_2 (S_{11}(q) - S_{22}(q) + \frac{c_2 - c_1}{c_1^{1/2} c_2^{1/2}} S_{12}(q)) \tag{10}$$

$$S_{CC}(q) = c_1 c_2 (c_2 S_{11}(q) + c_1 S_{22}(q) - 2c_1^{1/2} c_2^{1/2} S_{12}(q)). \tag{11}$$

The concentration–concentration structure factor $S_{CC}(q)$ is of a special importance: it is a measure for the concentration–concentration fluctuations in the liquids. For further details, see [16, 41]. Analogously, S_{NN} and S_{NC} correspond to the density–density and density–concentration fluctuations, respectively.

3.4. Densities of states and atomic charges

The density of states (DOS) describes the electronic structure of the system; it is defined as $n(E) \equiv \sum_i \delta(E - \varepsilon_i)$. For the calculation of the DOS, the δ-function $\delta(E - \varepsilon_i)$ is usually replaced by a δ_ε-function (normally a Gauss-type one).

Within plane-wave-based methods, like the CP one, one has direct and unambiguous access only to this total DOS. On the other hand, LCAO-based calculations yield in a very appealing way partial densities of states (PDOS) by splitting the DOS into fractions relating to particular basis functions or sets of basis functions—by a procedure which is very similar to what is known as Mulliken population analysis [35].

In particular, in our case it is possible to evaluate the contributions to the DOS from sodium and tin:

$$n_A(E) = \sum_{\mu}^{(\mu \in \mathrm{A})} \sum_i n_\mu^i \delta(E - \varepsilon_i) \tag{12}$$

with

$$n_\mu^i = \sum_\nu c_\mu^i c_\nu^i \langle \phi_\mu | \phi_\nu \rangle \tag{13}$$

where A denotes the atomic type (Na or Sn, respectively), i runs over the eigenstates and μ (and ν, respectively) count the LCAO basis functions ϕ_μ. The wavefunction expansion coefficients c_μ^i and the eigenvalues ε_i are the solutions of the secular equation (6) (see section 2.2). In the first equation the first summation runs over all LCAO basis functions which are centred at atoms of species A.

Since the LCAO scheme allows one to split up the DOS into fractions referring to *any* group of basis functions, it is not only possible to define an atomic-type-related PDOS but also PDOSs corresponding to s or p states—by considering the s and p basis functions, respectively, in equation (12).

To obtain the time average for the liquid, the DOS has to be averaged over the corresponding trajectory. However, it is not necessary to include *all* geometries of the trajectory to obtain the average, because consecutive time steps correspond to highly correlated configurations, between which the DOS does not vary substantially. It is sufficient to include 'well separated' configurations to ensure statistical independence of the configurational contributions to the average. In particular, we have chosen a time interval between the configurations in such a way that the mean squared displacement of the ions is about the size of the nearest-neighbour distance. Therefore, it was sufficient to take into account the DOS (or partial DOS) for six geometries for each composition, which leads to a significant saving of computing time.

The LCAO method allows one to calculate the (P)DOSs very quickly. Therefore we could calculate the (P)DOS considering not only six but also a larger number of configurations per trajectory. Comparing the (P)DOSs from six and sixteen configurations we found that the change is negligible. This means that it is indeed sufficient to take the trajectory average for just six 'well separated' configurations.

From the trajectory-averaged PDOSs relating to Na and Sn, one can obtain the time- and structure-averaged charge per Na and Sn atom, respectively, by integrating the particular PDOS up to the Fermi energy.

3.5. Electrical conductivity

The electrical (AC) conductivity for a given geometry is obtained using the Kubo–Greenwood (KG) formula [25]:

$$\sigma(\omega) = \frac{2\pi e^2}{3m_e^2\omega\Omega} \sum_m^{occ} \sum_n^{unocc} \sum_\alpha |\langle\psi_m|\hat{p}_\alpha|\psi_n)\rangle|^2 \delta(\varepsilon_n - \varepsilon_m - \hbar\omega) \tag{14}$$

where m_e and e are the electronic mass and charge, respectively, Ω is the MD cell volume and $\hat{p}_\alpha$ is the α-component of the momentum operator. The sum over m and n runs over occupied and unoccupied states, respectively—corresponding to the one-particle eigenvalues (from the Kohn–Sham equation) ε_m and ε_n as well as the one-particle wavefunctions ψ_m and ψ_n, respectively.

This formula may be compared with the 'joint density of states' with 'weight factors' $|\langle\psi_m|\hat{p}_\alpha|\psi_n)\rangle|^2$ for each contribution. When applying this formula, the δ-function needs to be smeared out again, like in the case of the density of states.

To obtain this conductivity for the liquid, one has to average $\sigma(\omega)$ over the whole trajectory of the MD 'production run'—in a similar manner to that for the structure factor or the DOS (see above). By carrying out this procedure, the effects of the ionic motion on the conductivity are implicitly considered. Finally, the extrapolation $\omega \to 0$ gives the desired DC conductivity.

As the Car–Parrinello method only yields the wavefunctions of occupied states (which are furthermore not the exact solutions of the Kohn–Sham equation—the system is only *near* the Born–Oppenheimer surface!), we had to evaluate the exact solutions ψ_m and ψ_n of the Kohn–Sham equations for each geometry considered. (The function $\sigma(\omega)$ depends rather sensitively on the accuracy of the wavefunctions!) To obtain reliable results, about 200 Kohn–Sham eigenstates had to be taken as input for the KG formula.

Hence, the computing time is high for the whole procedure described above, if one applies the *ab initio* method. However, again it is sufficient to take into account six 'well separated' configurations per trajectory, like for the densities of states, which can be understood on the basis of similar arguments (see the previous subsection). Within our LCAO scheme, the calculations with the KG formula can be performed very quickly. Thus we could again (like for the DOS) show that it is sufficient to take into account only a limited number of configurations. To obtain the DC conductivity, an extrapolation $\omega \to 0$ of $\sigma(\omega)$ had to be performed.

Finally, it should be noted that there are general warnings as regards the application of the KG formula within density functional theory (DFT), as follows.

(i) Zangwill and Soven [42] showed that one has, in principle, to include a 'local field' correction term within the Kohn–Sham formalism because the Kubo–Greenwood formula is correct for non-interacting electrons only. However, one can show [43] that this correction term vanishes for $\omega \to 0$. Hence, the ordinary KG equation should be correct for $\omega \to 0$ within the Kohn–Sham formalism.

(ii) Another (more heuristic) warning is that within the Kohn–Sham theory one has the so-called 'gap problem': the DFT does not yield the correct excited states in all cases and therefore gives wrong energy differences between occupied and unoccupied states. For a summary on calculations using the KG formula within DFT for liquids, see e.g. [15].

However, the systems considered by us are metals and semimetals—without real gaps; cf. the discussion of the densities of states in section 4. Indeed, general experience is [15] that the KG formula works well for metallic systems.

Overall, we expect the KG formula to give a reasonable description of the electrical conductivity for our systems.

4. Results

4.1. Structures

The calculated MD trajectories yield direct information about the structure in the liquids. We start our discussion with *ab initio* results obtained from CP simulations and add results from LCAO calculations at particular points.

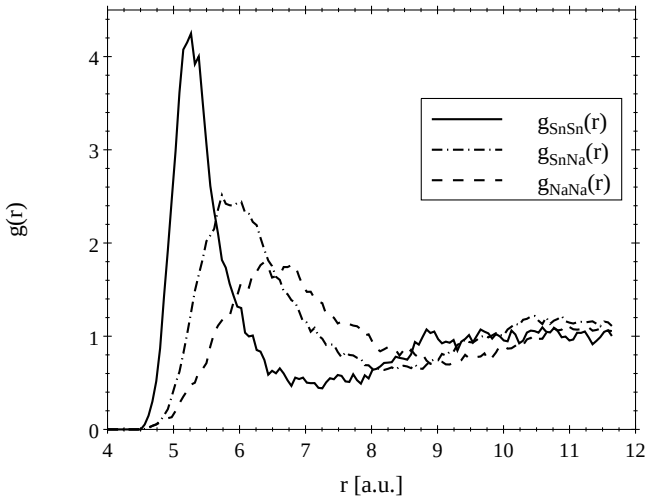

Figure 2. The pair correlation functions for equimolar NaSn at 921 K from the Car–Parrinello (CP) simulation. Shown are the Sn–Sn correlation (solid line), Sn–Na correlation (chain line) and Na–Na correlation (dashed line).

Figure 2 shows the trajectory-averaged pair correlation functions for the combinations Na–Na, Na–Sn and Sn–Sn for the composition with 50% sodium. The shapes of these curves are typical of a two-component liquid system. We obtained very similar plots for all of the other compositions.

Figure 3 shows characteristic configurations ('snapshots') of the liquids for three different compositions, taken from visualizations of the individual CP trajectories [44]. These visualizations show the following dynamic behaviour for the tin atoms.

(i) For the equimolar case (50% Na and Sn)—figure 3(b)—the Zintl anions Sn_4^{4-} do not survive as isolated clusters: they are destroyed and form networks. However, within these networks one can still observe tetrahedra-like substructures being formed and destroyed—i.e., there are highly *dynamical* networks. This is an important result, considering the fact that in many earlier investigations of these systems—for example, [16, 45]—it was assumed (or suggested) that these tetrahedra remain stable and isolated in the liquid. However, there is no clear support for this assumption.

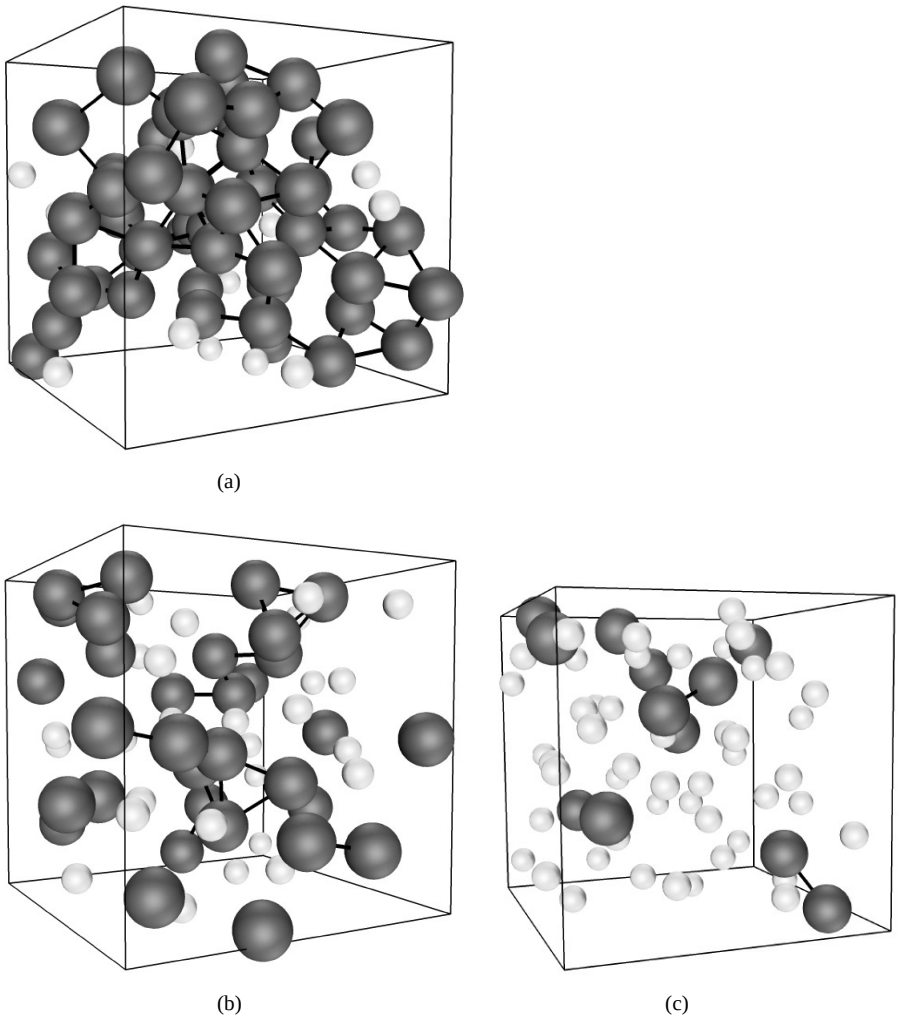

Figure 3. Snapshots of system configurations with 20% (a), 50% (b) and 80% (c) sodium. The Na atoms are plotted as smaller and lighter. The Sn–Sn bonds within the cut-off distance of 5.8 au are shown.

There are other studies supporting our conclusions: references [12] and [10] report on *ab initio* simulations of liquid equiatomic Cs–Pb and K–Si respectively (which are isovalent to NaSn). Here the same results were obtained: Pb and Si respectively form large networks in the melt.

A similar example of the formation of networks from a cluster-based solid-state structure is the transition from white to red phosphorus [46]: white phosphorus consists of P_4 clusters, which are isoelectronic to the Sn_4^{4-} Zintl anions. When heated up for some time, phosphorus turns from its white to its red modification, which is made up of large, disordered networks, similar to the situation that we observe for the tin-rich NaSn alloys.

The dynamics of the networks described above can be characterized by the fluctuations in the Sn–Sn coordination numbers over time. These numbers give the Sn neighbours around each Sn atom within a bonding distance which we have chosen from the Sn–Sn

pair correlation functions (figure 2) to be 6 au. This coordination number shows a strong fluctuation over time. About one half of the tin atoms are threefold coordinated (which is similar to the situation in the tetrahedra, i.e., in the solid); about one quarter are twofold and fourfold coordinated. The latter case corresponds to the situation in the network.

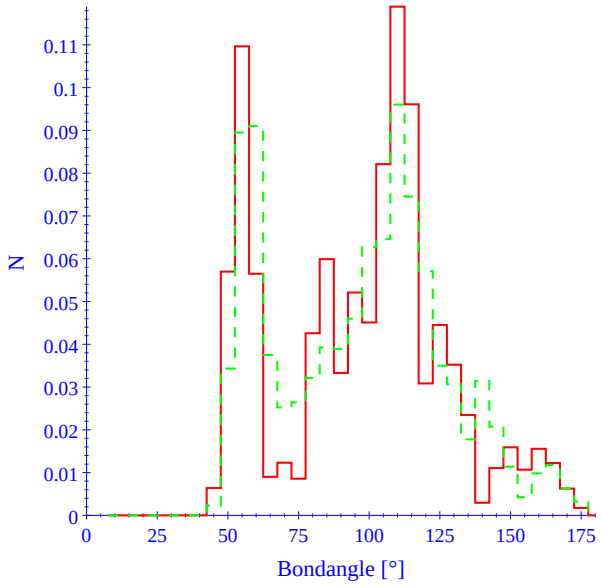

Figure 4. The bond-angle distribution for equimolar NaSn at 921 K calculated with a cut-off radius of 6 au. The solid line refers to fourfold-coordinated atoms, the dashed line to threefold-coordinated atoms. Note the two distinct maxima at the tetrahedra angles of 60° and at 109° referring to network atoms.

The network formation of surviving or rebuilt tetrahedra (or relics of them) is also reflected in the angle distribution of the Sn–Sn–Sn bonds; see figure 4, where the contributions from the threefold- and fourfold-coordinated Sn atoms are also given. The first maximum in all cases—at 60°—is the bond angle within Sn_4 tetrahedra or the remaining pieces of them. The second maximum—at 109°—comes from the fourfold nearly tetrahedrally coordinated atoms. The first maximum indicates that many of the tin atoms remain in a local tetrahedra-like environment, whereas in the more extended surrounding they form large and dynamic networks, for which the second maximum is an indication.

To rule out the possibility that our results are artefacts due to the use of a finite and cubic supercell, we performed additional simulations with larger supercells containing 216 atoms and also with the original orthorhombic cell with 64 atoms (cf. section 3.1 and figure 1). However, for these simulations we could not apply the *ab initio* CP method but used the LCAO method. The results from these LCAO-scheme-based simulations for the 64-atom supercell as well as for the 216-atom supercell and the orthorhombic cell are essentially the same as from the CP calculations.

Furthermore, we checked the influence of temperature and supercell parameters.

However, we obtained (from CP simulations) that the change of the above-discussed (dynamic) properties (including the structure factors; see below) is very small—within the statistical error—(i) for temperature deviations of ±100 K and (ii) for deviations of the basis length of the supercell of about 10% (which is within the expected pseudopotential

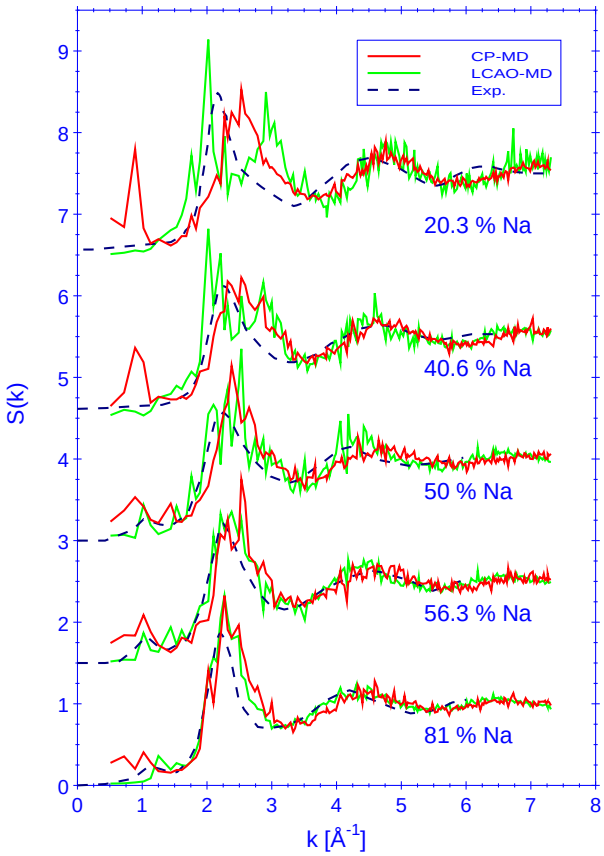

Figure 5. Structure factors for different compositions of NaSn alloys obtained by means of CP and LCAO simulations compared with those derived from neutron scattering experiments.

error of the equilibrium lengths; see section 3.1).

For the composition with 43% tin the situation is very similar.

(ii) For higher tin concentrations (60 and 80% tin)—figure 3(a)—these networks become denser and more rigid, but also show fluctuations in the coordination numbers. We observe only a few atoms with more than fourfold coordination and less than twofold coordination.

(iii) When the content of tin is reduced to 20%, neither networks nor Zintl anions can be observed; see figure 3(c). Instead we find that the isolated tin atoms and dimers are preferred. The dimers are stable—with oscillations of the bond lengths around 5.5 au and without a noticeable trend towards separation.

Furthermore, we investigated for this composition the existence and the stability of the so-called 'octet compounds' ($SnNa_4$ clusters—related to CH_4, for example), which were suggested e.g. by Alblas *et al* [16]. For this analysis, the Na–Sn–Na bond angles and coordination numbers were investigated. However, we did not find any evidence for the existence of such complexes.

4.2. Structure factors

The calculated structure factors (from the CP and LCAO simulations for the same cell sizes) are presented and compared with the experimental values [16] in figure 5. The positions of the peaks (including the prepeak and the first minimum after the first main peak) as a function of the composition were given in reference [23]. As can be seen, the agreement between the experimental and theoretical curves is good. In particular, the trends of the peak positions are reproduced correctly. However, the positions of the main peaks of the CP structure factors are slightly shifted towards larger k-values. This is a pseudopotential effect: in the pseudopotential calculations the bond lengths tend to come out slightly too small; this corresponds to too large k-values in reciprocal space.

The prepeaks are in the correct positions. However, for small Na concentrations (20 and 40%) no sharp prepeaks were measured, whereas we obtain large prepeaks from CP simulations, but not from LCAO-MD.

The interpretation of the origin of the prepeaks in the structure factors is not unequivocal and there is controversy in the literature [48–50].

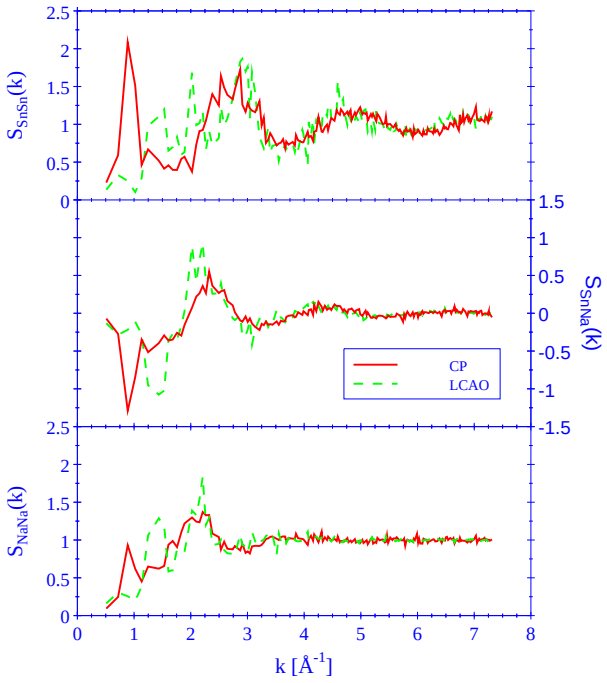

Figure 6. Partial structure factors according to Ashcroft and Langreth [40]—see equation (8)—for the composition with 60% tin from the CP simulation.

Apart from the interpretation as intermediate-range order (IRO) effects, they could also be attributed to finite-size effects (finite supercells and finite simulation times). However, in LCAO simulations with the same supercell and its enlarged (216 atoms) counterpart the prepeak disappears for the tin-rich compositions (80 and 60% Sn and 20 and 80% Na), but persists for the other three. Hence, these LCAO results are in agreement with the experiments and give a better confidence that the prepeak is not due to finite-size effects. Furthermore, one might argue that the structure factor is most affected in the low-k region by the statistical error of the simulation, but the partial structure factors (Ashcroft–

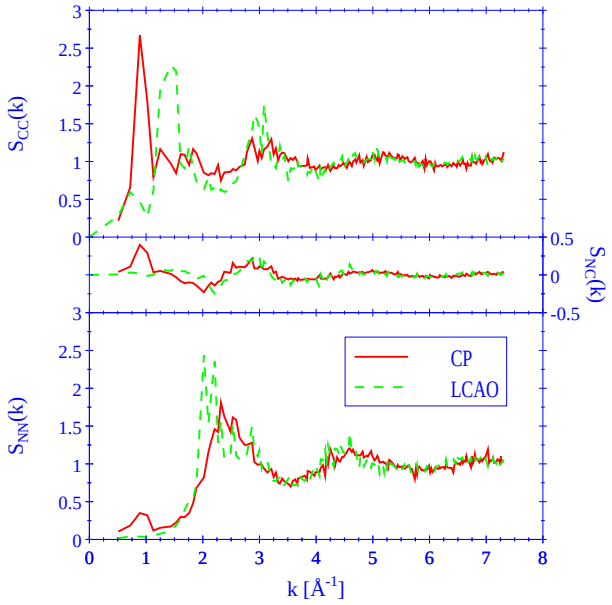

Figure 7. Partial structure factors according to Bhatia and Thornton [41]—see equations (9)–(11)—for the composition with 60% tin from the CP simulation.

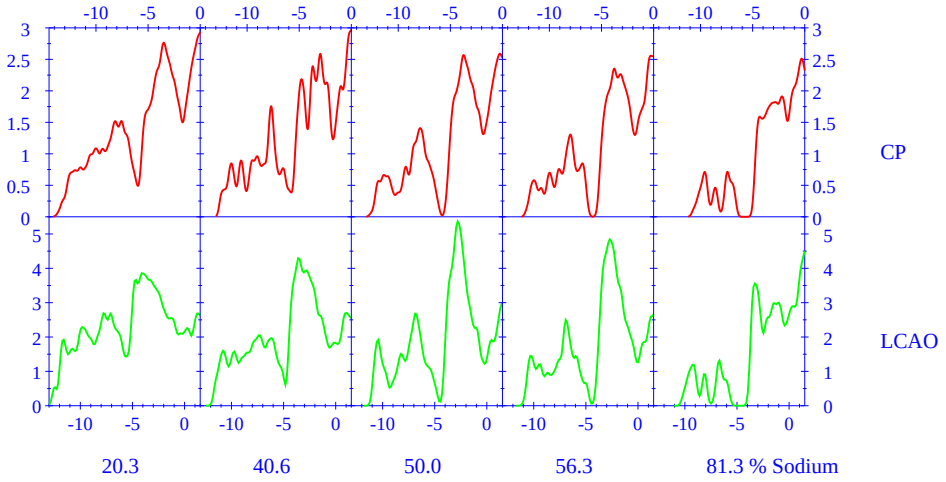

Figure 8. Densities of states calculated within the CP (top row) and within the LCAO (bottom row) scheme for different liquid NaSn alloys, calculated as ensemble averages over CP trajectories.

Langreth—figure 6; Bhatia–Thornton—figure 7) show clearly that the prepeak is not caused by statistical noise effects. We find that the most dominant contribution to the prepeak comes from the $S_{\mathrm{Sn-Sn}}$-part (figure 6) of the Ashcroft–Langreth structure factors, or from the S_{CC}-part according to the Bhatia–Thornton split-up (figure 7), respectively. S_{CC} describes the concentration fluctuations [22] in a system and thus measures the ordering of the two species in the (liquid) system.

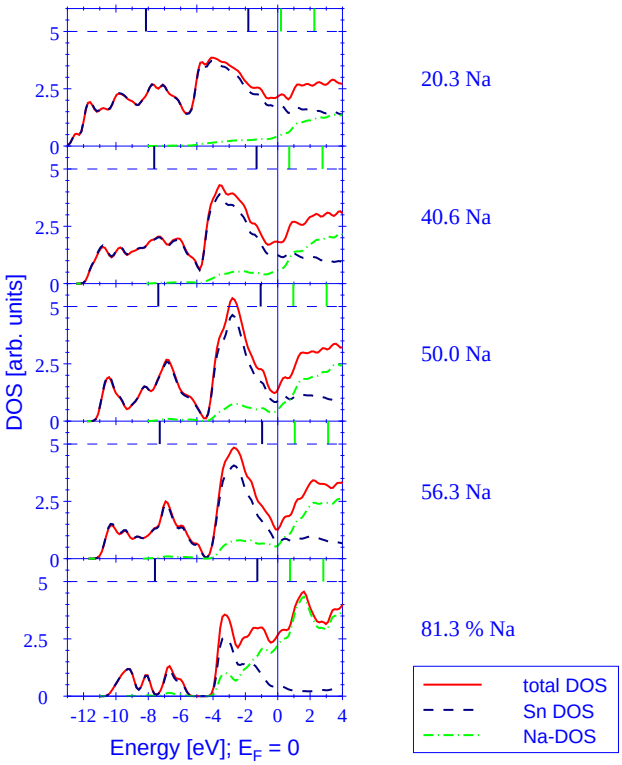

Figure 9. The total density of states (DOS) and partial densities of states (PDOSs) showing contributions from sodium and tin. Both the DOS and the PDOSs are calculated within the LCAO scheme as ensemble averages from data taken from *ab initio* CP trajectories. The Fermi energy is set to be zero.

Hence, the prepeak appears to be a result of some intermediate-range ordering within the tin subsystem. This could be due to some kind of interlayer correlation of the Sn networks (cf. [47]). But analysing the CP and LCAO-MD trajectories one finds that the tin networks are stiffer and less structured in LCAO-MD, whereas they show more fluctuations and structuring in the CP simulations. Within these fluctuations, more relics of the original tetrahedral structure are visible. This is due to a slight underestimation of the tin–tin interaction by CP simulation on the one hand and an overestimation within the LCAO scheme on the other. This overestimation also causes problems with the fluidity of the tin-rich compositions in LCAO-MD, which can be seen in a broadening and structuring of the main peak of the corresponding structure factors

Thus, the prepeak is connected with correlations between the remaining tetrahedral structures within the tin networks.

4.3. Electronic structure: densities of states and atomic charges

The trajectory-averaged total densities of states, calculated by means of the CP and LCAO methods, are presented for each composition in figure 8. The DOSs are both based on the same CP trajectory (cf. table 1).

As can be seen, there is a qualitative agreement between the CP- and LCAO-based data.

Deviations between the two sets of results are small and are mostly located at energies above the Fermi level. This is due to the small limited (sp-only) basis sets of the LCAO method, which does not describe the higher-lying levels as accurately as the plane-wave basis does.

Although there are also differences between the results from the two methods around the Fermi energy and below, in this region we have an overall qualitative agreement, especially concerning the changes in the DOS from one composition to another. This allows us to use the LCAO-based partial DOSs (PDOSs) for a qualitative discussion of the change in conductivities with the Sn concentration.

The PDOSs, corresponding to Na and Sn contributions (together with the total DOS from LCAO), are presented for all of the compositions in figure 9. In the uppermost part of each panel the atomic Kohn–Sham energies for the Na and Sn s and p states are shown. As can be seen, the basic shape of the DOS is similar in all plots. We have areas dominated by the different types of basis functions corresponding to the atomic Kohn–Sham energies.

The high-energy part of the DOS is mainly made up of contributions from Na-centred basis functions. The group of peaks at very low energies ($\geqslant$ 4 eV below E_F) is mainly due to Sn s basis functions. In between is an area which is characterized by the transition from a DOS dominated by Sn p to a DOS determined by Na basis functions.

Within this transition the Fermi energy moves from the tin-dominated towards the sodium-dominated side of the DOS, as the sodium concentration is increased. This behaviour is important for the discussion of the changes in quantities such as the conductivity (see subsection 4.4).

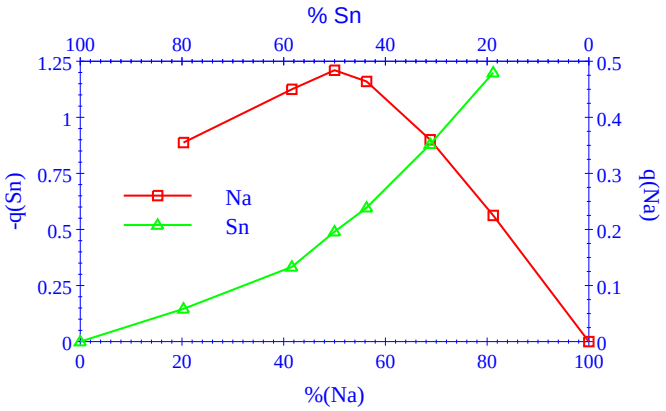

Figure 10. Mean atomic charges of Na and Sn, respectively, as functions of composition for liquid NaSn, from the integration of the PDOSs up to the Fermi energy.

Figure 10 shows the mean atomic charges for the different compositions, which were obtained by integrating the individual PDOSs up to the Fermi energy. These time-averaged and structure-averaged charges per atom measure the charge transfer between the two components of the system and thus may be used to characterize the type of bonding in the system.

For the tin-rich systems the charge transfer increases almost linearly with the sodium concentration. Near the equimolar composition the charge transfer reaches its maximum. Hence, the nearly equimolar systems are mostly made up of ionic bondings. A further increase in the Na concentration leaves the tin atoms highly coordinated with sodium. Due to the difference in electronegativity, tin attracts electrons from the surrounding sodium and thus increases its averaged (negative) charge. However, as a consequence of the

concentration ratios, the averaged (positive) charge of sodium decreases. Thus, the electron concentration in the sodium subsystem is higher than it was in the equimolar case (E_F moves into the sodium sp energy band). Hence, a metallic-like sodium subsystem can be formed.

This corresponds to a metallic like tin subsystem for the tin-rich compositions.

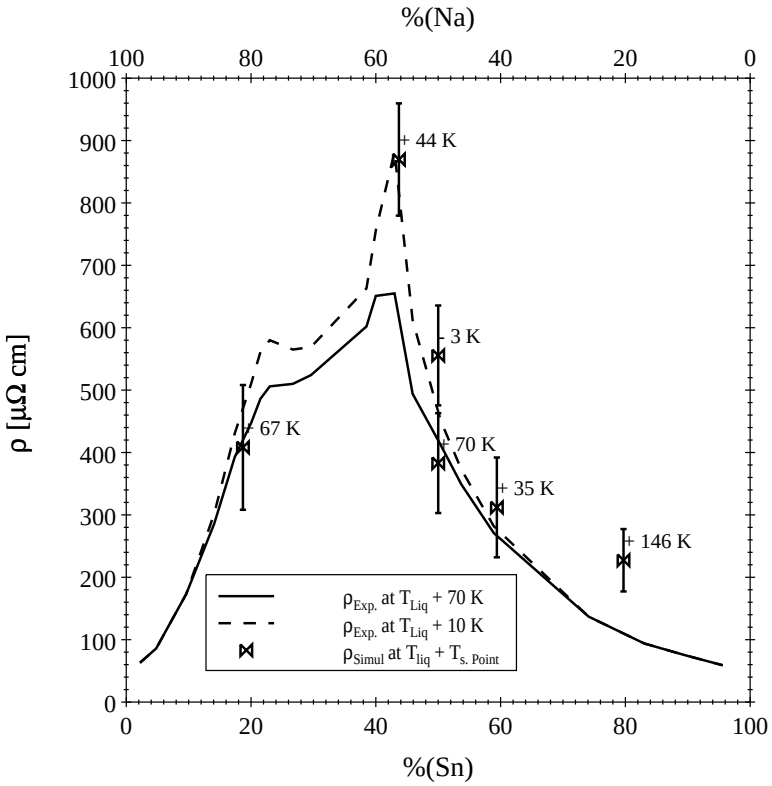

Figure 11. The variation of the DC resistivity for liquid NaSn alloys with composition. Shown are experimental data taken from [19] for 70 K above the melting point and values calculated within this work.

4.4. Electrical conductivity

The electrical conductivity as a function of frequency ($\sigma(\omega)$) is calculated by the Kubo–Greenwood (KG) formula for the CP trajectories of all of the compositions. The extrapolated values $\sigma(0)$ give the DC conductivities [51]—see also [24].

The shape of $\sigma(\omega)$ indicates a non-Drude-like behaviour, which reflects the non-free-electron-like nature of the electronic states.

The corresponding calculated resistivities $\rho = 1/\sigma(0)$ are drawn in figure 11 for comparison with the experimental data of van der Marel *et al* [19]. As can be seen, the strong dependence of the conductivity on the composition is reproduced very nicely: for compositions close to pure sodium and tin we obtain small resistivities, whereas near the equimolar composition the high semimetallic (almost semiconducting) resistivity is reproduced. For the case with 20% Na we obtain a larger mismatch between the

experimental and calculated resistivity. However, also for this case, the trend towards a small (metallic) resistivity is reproduced correctly.

The errors in figure 11 have three sources: (i) the statistical noise due to there being a finite number of states, i.e. due to the use of a finite supercell; (ii) the enhancement of the noise for small denominators ω; and (iii) the noise due to the configurational average being over a finite number of geometries of the trajectory. Related to these errors, an additional source of uncertainty is the extrapolation towards zero frequency.

Furthermore, it should be noted that there are also small deviations of the temperatures of our CP simulations—given in table 1—from the experimental temperatures, which are 70 K above the corresponding melting point [19]. In addition to this, small deviations may also result from the fact that the experimental equilibrium volume that is used is reproduced by our pseudopotentials only within 10%. Finally, some errors may be due to the general problems concerning the applicability of the KG formula within DFT. However, these errors should be small for metals; see section 3.5 and [15].

The DC resistivities obtained from both LCAO and *ab initio* (CP) calculations are given in table 2. (As for the calculation of the DOSs, we used for reasons of comparability the CP trajectories for the LCAO calculations.) As can be seen, the CP results agree better with the experiments. This is due to the fact that for the plane-wave basis (used in the CP method) the unoccupied states, in particular, are described much more precisely than within the LCAO scheme.

Table 2. Resistivities of NaSn alloys with different compositions, in $\mu\Omega$ cm.

% Na	Experimental [19]	CP, calculated	LCAO, calculated
20	110 ± 0.2	227 ± 50	230 ± 80
40	274 ± 1	312 ± 80	400 ± 100
50	426 ± 5	383 ± 80	800 ± 200
57	658 ± 10	869 ± 90	850 ± 200
80	426 ± 5	408 ± 100	180 ± 100

The strong dependence of the conductivity on the composition can be understood qualitatively on the basis of the partial densities of states and the mean atomic charges—see figures 9 and 10 and the discussion in section 4.3.

As mentioned there, the contribution of each component to the DOS near the Fermi level changes with composition: the more sodium is added, the more the DOS at the Fermi level is dominated by contributions from sodium. Furthermore, the position of the Fermi level within the DOS shifts towards higher energies as the sodium concentration increases.

For compositions with a small content of sodium, the Fermi energy lies in the region dominated by tin—with a large DOS at the Fermi energy, corresponding to a high (metallic) conductivity. This refers to the dominance of Sn metallic bonding in these systems; cf. the discussion of figure 10.

For compositions with 50 and 57% sodium, the Fermi level is out of the tin-dominated region, but still has not reached the sodium-dominated area. This yields a small DOS for these cases (nearly a pseudogap) at the Fermi level. Therefore, one gains an understanding of the minimum of the conductivity, i.e. for the maximum of the resistivity near the equimolar composition. For solid equimolar β-NaSn, there is even a gap at the Fermi level (between two sets of states dominated by tin and sodium, respectively) [18]. For these systems the maximum in resistivity is in accord with the fact that for these systems the bonding type is mostly ionic—see figure 10.

In compositions with excess sodium the situation changes again: the Fermi level is in the sodium-dominated region, yielding again a large DOS at the Fermi energy and a metallic conductivity like in the tin-rich cases. This again matches the picture of the dominance of metallic-like bondings for these compositions (see figure 10).

These results can be compared with earlier investigations of Geertsma [4], who applied a tight-binding model for liquid alloys of alkali metals with group-IV elements. Using the content of isolated group-IV atoms (i.e. Sn in our case) as an input parameter, he obtained the DOS at the Fermi level as a function of composition (see figure 13 in [4]).

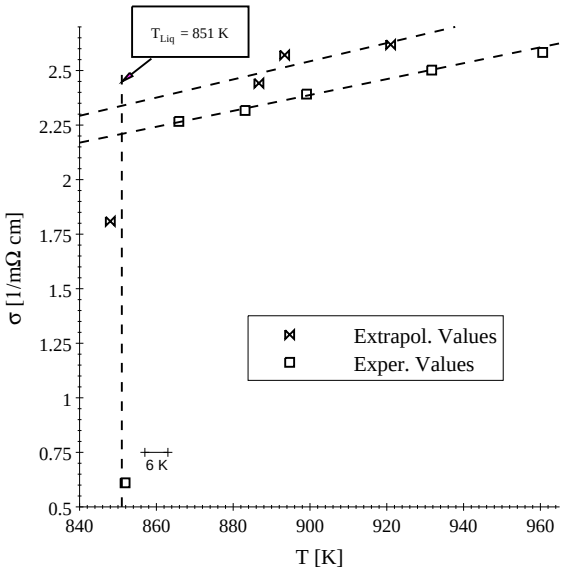

Figure 12. The temperature dependence of liquid equimolar NaSn. Shown are experimental values taken from [20] (squares) and values calculated as ensemble averages from CP simulations (triangles).

We can extract this content of isolated tin atoms from our CP trajectories. It varies from about 3% for the tin-rich alloys up to 50% for the sodium-rich case. Using these numbers, we get the same trend as shown by Geertsma.

(i) The total DOS has a minimum in the region around 50% sodium.

(ii) The partial DOS corresponding to Na is nearly constant for 0–60% Na and then grows monotonically with the Na content.

Similarly to Geertsma [4], we find some tendency for clustering of Sn atoms near the equimolar composition. But militating against the assumption of ideal isolated Sn_4 tetrahedra as proposed by Geertsma, we observe this clustering only as fluctuations of the tin networks—see section 4.1.

As already mentioned above, deviations between our calculations and the experimental resistivities may be due to the different temperatures of the experiment and simulation. Experiments show a noticeable temperature dependence of the resistivity, especially around the equimolar composition [16, 20].

To investigate this dependence, we calculated the (Kubo–Greenwood) conductivity of equimolar NaSn for a set of four different temperatures. In figure 12 the experimental conductivities as a function of temperature taken from [20] (marked with squares) are

compared to results from our CP-MD simulations (triangles). Additionally the liquidus point T_{liq} is marked. As can be seen, we obtain the correct behaviour: the conductivity grows with temperature. In particular, for temperatures immediately above T_{liq} the calculated conductivity shows the typical linear enhancement expected for semiconducting materials. The calculated values are about 5 to 10% above the experimental curve.

Around the melting point the measured conductivity changes by several orders of magnitude. Indeed, in figure 12 our calculated value for the lowest temperature shows the onset of this dramatic change. It should be noted that the experimental melting point (851 K; see also table 1) is slightly above this lowest simulated temperature (848 K). However, from our tests of the 'liquidity' (see section 3.2) we conclude that the 848 K simulation still represents the liquid state of NaSn. Hence, the liquidus point for our simulations is at least about 6 K below its experimental value. Introducing such a temperature shift in figure 12 would further decrease the difference between the conductivities from experiment and our simulations to about 3 to 7%.

Thus, our results are in agreement with experimental findings. We even find indications for the very fast change in the electronic properties close to the liquid–solid transition.

5. Summary

We have considered liquid sodium–tin alloys in five different compositions by first-principles calculations. We performed *ab initio* density functional molecular dynamics simulations within the Car–Parrinello (CP) scheme for supercells with 64 atoms and with a simplified LCAO method for supercells with 64 and 216 atoms.

The trajectories of the molecular dynamics simulations yield direct information about the structures in the liquids and about the structure factors. For the investigation of the structural properties we considered the pair correlation functions, the angular distribution and the coordination numbers; furthermore, a video was produced to aid visualization.

An essential result is that—for the equimolar case—the so-called Zintl anions Sn_4^{4-}, appearing in the solid β-NaSn, cannot be found in the melt. They are destroyed and form dynamic networks. In the case of sodium-rich alloys, only isolated tin atoms or dimers occur. These dimers are stable and oscillate. The 'octet compounds' $SnNa_4$, which have been suggested for sodium-rich alloys by some authors, could not be observed.

The structure factors from our trajectories agree qualitatively with experimental data including the prepeaks—apart from the prepeaks for compositions with a high content of tin, which are not observed in the experiments, whereas we obtain them from the CP (but not from the LCAO) calculations.

The prepeak for the liquid tin-rich compositions in CP simulations is due to correlations between remaining fragments of the Sn_4^{4-} Zintl tetrahedra, which are dominant in the solid phase of equimolar β-NaSn. These correlations are overestimated within the CP scheme, whereas in LCAO calculations the tin–tin interactions are somewhat too strong. Thus in LCAO simulations the tin networks are more static and unstructured than in CP simulations, which results on the one hand in a suppression of the prepeak, but on the other hand gives rise to problems with the fluidity of the system, which shows up in a broad structured main peak in $S(k)$.

The DC electrical conductivities calculated by means of the Kubo–Greenwood formula using the Car–Parrinello trajectories agree very well with the experiments and reproduce the very strong variation with composition ranging from metallic to almost semiconducting behaviour. This can be understood by considering the partial densities of states. Our results concerning the total densities of states at the Fermi energy agree, in principle, with earlier

results of Geertsma obtained using a tight-binding model.

Furthermore, the temperature dependence of the conductivity could be reproduced within an error of about 5%, including the dramatic change close to the liquid–solid phase transition.

The problems connected with the application of the Kubo–Greenwood formula are discussed in detail. As an alternative, one could take the limit $\omega \to 0$ in equation (14) analytically to obtain the DC conductivity. This requires the smallest finite energy difference between the highest occupied and the lowest unoccupied state to be very small. The resulting formula

$$\sigma(0) = [(2\pi e^2\bar{h}^3)/(3\Omega m^2)]N^2(E_F)\sum_{\alpha}|\langle\psi_1|p_\alpha|\psi_2\rangle|^2$$

directly yields the DC conductivity and thus saves one from having to extrapolate the noisy data. However, first tests within our LCAO scheme showed that one needs to take into account many more configurations per trajectory to get adequate statistics for reliable results. Hence, it remains to be established whether or not this formula is a fast alternative to the ordinary Kubo–Greenwood equation.

To check the limitations of the finite supercell (connected with a broad k-mesh and possible 'superstructure effects'), the simulations were repeated for larger supercells—applying the LCAO method. The results from these simulations support our conclusions reached with the smaller cells. Hence, the supercells with 64 atoms should be large enough. The conductivities from the LCAO calculations agree with the experiments only qualitatively because the Kubo–Greenwood formula needs very accurate wavefunctions. Additionally, there are some deviations in the total DOSs between the CP and LCAO results arising from basis set effects.

Other limitations of our methods are: (i) the finite simulation time causing statistical noise; (ii) the (small) deviations between the theoretical and experimental equilibrium lengths and volumes—which is due to the pseudopotential being adopted without the non-linear core corrections to economize on time; and (iii) deviations between the experimental and theoretical temperatures; cf. table 1. However, the measured and calculated structure factors depend only very weakly on temperature and vary only within the statistical noise of our simulations.

Furthermore, the sodium–antimony system was simulated by us recently [52]. Here, the Zintl anions are (for the equimolar case) tellurium-like spiral chains of antimony atoms. We find that these chains are destroyed in the melt—similarly to the case for Zintl anions in NaSn; these chains survive piecewise and form new networks.

Acknowledgments

We gratefully acknowledge support from the Deutsche Forschungsgemeinschaft (DFG) and the Max-Planck-Institut für die Physik komplexer Systeme, Dresden. Parts of the calculations were performed on the Cray systems of the Centro Interdipartimentale di Calcolo dell' Università di Trieste and of CINECA at Bologna. GP acknowledges the CNR for financial support: Contributo di ricerca No 95.00505.CT12.

References

[1] Zintl E and Brauer G 1933 *Z. Phys. Chem.* B **20** 245
Zintl E and Woltersdorf G 1935 *Z. Elektrochem.* **41** 876
Zintl E 1939 *Angew. Chem.* **52** 1
[2] Kauzlarich S M (ed) 1996 *Chemistry, Structure, and Bonding of Zintl Phases and Ions* (New York: VCH)

[3] Geertsma W, Dijkstra J and van der Lugt W 1984 *J. Phys. F: Met. Phys.* **14** 1833
[4] Geertsma W 1985 *J. Phys. C: Solid State Phys.* **18** 2461
[5] Geertsma W 1990 *J. Phys.: Condens. Matter* **2** 8517
[6] van der Lugt W 1996 *J. Phys.: Condens. Matter* **8** 6115
[7] Reijers H T J, Saboungi M-L, Price D L, Richardson J W Jr, Volin K J and van der Lugt W 1989 *Phys. Rev.* B **40** 6018
[8] Reijers H T J, van der Lugt W and Saboungi M-L 1990 *Phys. Rev.* B **42** 3395
[9] Geertsma W and Saboungi M-L 1995 *J. Phys.: Condens. Matter* **7** 4803
Stolz M, Winter R, Howells W S and McGreevy R L 1995 *J. Phys.: Condens. Matter* **7** 5733
[10] Galli G and Parrinello M 1991 *J. Chem. Phys.* **95** 7054
[11] de Wijs G A, Pastore G, Selloni A and van der Lugt W 1993 *Phys. Rev.* B **48** 13 459
[12] de Wijs G A, Pastore G, Selloni A and van der Lugt W 1994 *Europhys. Lett.* **27** 667
de Wijs G A, Pastore G, Selloni A and van der Lugt W 1995 *J. Chem. Phys.* **103** 5031
[13] de Wijs G A, Pastore G, Selloni A and van der Lugt W 1996 *J. Phys.: Condens. Matter* **8** 1879
[14] Holender J M and Gillan M J 1996 *Phys. Rev.* B **53** 4399
[15] Kirchhoff F, Holender J M and Gillan M J 1996 *Phys. Rev.* B **54** 190
[16] Alblas B P 1983 *Thesis* Groningen University
Alblas B P, van der Lugt W, Dijkstra J, Geertsma W and van Dijk W 1983 *J. Phys. F: Met. Phys.* **13** 2465
[17] Müller W and Volk K 1977 *Z. Naturf.* b **32** 709
Müller W and Volk K 1978 *Z. Naturf.* b **33** 275
[18] Springelkamp F, de Groot R A, Geertsma W, van der Lugt W and Müller F M 1985 *Phys. Rev.* B **32** 2319
[19] van der Marel C, van Oosten A B, Geertsma W and van der Lugt W 1982 *J. Phys. F: Met. Phys.* **12** 2349
[20] Fortner J, Saboungi M-L and Enderby J E 1995 *Phys. Rev. Lett.* **74** 1415
[21] Price D L, Saboungi M-L and Howells W S 1995 *Phys. Rev.* B **51** 14 923
Stoddard R D, Conradi M S, McDowell A F, Saboungi M-L and Price D L 1995 *Phys. Rev.* B **52** 13 998
[22] Seifert G, Pastore G and Car R 1992 *J. Phys.: Condens. Matter* **4** L179
[23] Schöne M, Kaschner R and Seifert G 1995 *J. Phys.: Condens. Matter* **7** L19
[24] Kaschner R, Schöne M, Seifert G and Pastore G 1996 *J. Phys.: Condens. Matter* **8** L653
[25] Economou E N 1983 *Green's Functions in Quantum Physics (Springer Series in Solid State Sciences 7)* (Berlin: Springer) p 152ff
[26] Car R and Parrinello M 1985 *Phys. Rev. Lett.* **55** 2471
[27] Porezag D, Frauenheim Th, Köhler Th, Seifert G and Kaschner R 1995 *Phys. Rev.* B **51** 12 947
Seifert G, Porezag D and Frauenheim Th 1996 *Int. J. Quantum Chem.* **58** 185
[28] Hohl D 1992 *Density Functional Theory Workshop, Cornell Theory Center* (Ithaca, NY: Cornell University Press)
[29] Perdew J P and Zunger A 1981 *Phys. Rev.* B **23** 5048
[30] Bachelet G B, Hamann D R and Schlüter M 1982 *Phys. Rev.* B **26** 4199
Hamann D R 1989 *Phys. Rev.* B **40** 2980
[31] Silvestrelli P, Alavi A and Parrinello M 1997 *Phys. Rev.* B **55** 15 515
[32] Huber K P and Herzberg G 1979 *Constants of Diatomic Molecules* (New York: Van Nostrand)
[33] Boerrigter P M, te Velde G and Baerends E J 1988 *Int. J. Quantum Chem.* **33** 87
te Velde G and Baerends E J 1992 *J. Comput. Phys.* **99** 84 and references therein
[34] Louie S G, Froyen S and Cohen M L 1982 *Phys. Rev.* B **26** 1738
[35] Mulliken R S 1955 *J. Chem. Phys.* **23** 1833
[36] The Slater–Koster tables and the data for the repulsive potentials for the atomic combinations Na–Na, Na–Sn and Sn–Sn are available upon request from the authors.
[37] Biltz W and Weibke F 1935 *Z. Anorg. Allg. Chem.* **223** 321
[38] Van den Broek J J 1972 *Phys. Lett.* **40A** 219
[39] Hansen M and Anderko K 1979 *Constitution of Binary Alloys* (New-York: McGraw-Hill)
[40] Ashcroft N W and Langreth D C 1967 *Phys. Rev.* **156** 685
[41] Bhatia A B and Thornton D E 1970 *Phys. Rev.* B **2** 3004
[42] Zangwill A and Soven P 1980 *Phys. Rev.* A **21** 1561
[43] Kaschner R, unpublished
[44] To get an impression of the structures in the liquid and on how these structures change, we produced a video of the MD-simulated trajectories. The video is available on request from the authors.
[45] Geertsma W and Saboungi M-L 1995 *J. Phys.: Condens. Matter* **7** 4803
[46] Hohl D and Jones R O 1994 *Phys. Rev.* B **50** 17 047
[47] Boos A, Steeb S and Godel D 1972 *Z. Naturf.* a **27** 271

[48] Nakano A, Kalia R K and Vashishta P 1994 *J. Non-Cryst. Solids* **171** 157
[49] Cao Y, Cormack A N, Clare A G, Bachra B, Wright A C, Sinclair R N and Hannon A C 1994 *J. Non-Cryst. Solids* **177** 317
[50] Fayos R, Bermejo F J, Dawidowski J, Fischer H E and González M A 1996 *Phys. Rev. Lett.* **77** 3823
[51] It should be mentioned that the results for $\sigma(\omega)$ are isotropic values: the KG formula (14) is an average of contributions from three directions of real space ($\frac{1}{3}\sum_\alpha$; $\alpha = x$, y, or z). Comparing these three contributions, we found that the individual results agree within the statistical noise. This isotropy may be viewed as a further indication of the fluidity of the system. However, the average over the directions α further reduces the statistical error.
[52] Kaschner R and Seifert G 1998 *J. Phys.: Condens. Matter* at press